AIChE

A Dynamic Buildup Growth Model for Magnetic Particle Accumulation on Single Wires in High-Gradient Magnetic Separation

Fei Chen, Kenneth A. Smith, and T. Alan Hatton
Dept. of Chemical Engineering, Massachusetts Institute of Technology, Cambridge, MA 02139

DOI 10.1002/aic.12809
Published online December 9, 2011 in Wiley Online Library (wileyonlinelibrary.com).

Magnetic fluids containing nano or submicron magnetic particles and their applications to food, biological, and pharmaceutical systems have recently attracted considerable attention. Magnetic particles can be collected efficiently in magnetizable matrices (e.g., iron wires) in high-gradient magnetic separation processes. However, capture efficiencies based on results for clean, particle-free, wires may be seriously in error because the particle accumulation on the wire distorts the flow and the magnetic fields, and thus influences the capture efficiency. A model is developed here in which the dynamic growth process is treated as a moving boundary problem, with the growing front tracked explicitly by marker points distributed evenly over its surface. The flow field and magnetic field are calculated using a finite element method, and a particle trajectory model is used to calculate the deposition flux on the surface. The marker point distribution and the buildup shape are updated at each simulation step. Simulation results show that, for weakly magnetic particles, the accumulation exhibits a smoothly growing front, whereas for strongly magnetic particles, an instability occurs, leading to dendritic growth. The capture efficiency decreases dramatically as particle accumulation increases; and this trend is more prominent for the transverse configuration than it is for the longitudinal configuration. The simulation results show good agreement with experimental results from the literature. © 2011 American Institute of Chemical Engineers *AIChE J*, 58: 2865–2874, 2012

Keywords: high gradient magnetic separation, magnetic particles, particle accumulation, front-tracking, dendritic growth

Introduction

High-gradient magnetic separation (HGMS) is used for the concentration, removal, and fractionation of magnetic particles from fluid streams. It has been applied to the beneficiation of metal ores,[1] the recovery of metals from wastes,[2] and waste water treatment in the steel industry and in thermal power plants.[3] Recently, HGMS processes together with the use of functionalized magnetic particles have been extended to more complex systems, such as cell manipulation,[4,5] protein separation,[6–10] heavy metal ion[11] and nonpolar organic contaminant[12] removal from water streams, and analytical applications.[13] Low cost, high selectivity, excellent operational flexibility, and ability to treat highly complex feedstocks all make HGMS a promising technique for these applications relative to traditional adsorption techniques, including chromatography and expanded bed adsorption.

For particles comprised of a soft magnetic material, the magnetic force is given by:[14]

$$\mathbf{F_M} = \mu_0 V_p M_p \nabla H \tag{1}$$

where μ_0 is the free space permeability, V_p is the particle volume, M_p is the volumetric magnetization of the particle material which is equal to the particle density ρ_p multiplied by the particle mass magnetization σ_{sp}, and H is the scalar value of the magnetic intensity at the location of the particle. For a magnetic particle to be separated from the stream, the magnetic force must compete successfully with other external forces due to gravity, hydrodynamic drag, and Brownian thermal motion. Typically, magnetizable wires (usually of stainless steel) are placed inside the separator to induce high-magnetic field gradients and, therefore, high magnetic forces.

Various theoretical approaches have been used to aid in the understanding, design, and optimization of HGMS processes. For example, particle trajectory and trapping models have been used to study the migration and capture of large magnetic particles and nonmagnetic particles by single-wire and multi-wire matrices subject to magnetic, flow, and other external force fields.[15–17] Although these models are still widely used,[18] they assume clean wires (particle-free) and, because they do not account for the effect of particle accumulation on the wires, they are applicable only at the very early stages of the capture process. However, the reality is that, as the particle buildup grows, it modifies the effective geometry of the wire and consequently influences the flow and magnetic fields.[15]

A simplified model that is able to predict the maximum particle accumulation on a wire has been developed and tested experimentally by Liu and Oak[19] and Nesset and Finch.[20] In this model, the interface is assumed to remain cylindrical at all times, and potential flow theory is invoked to obtain the flow field around the wire. There is a critical value

Correspondence concerning this article should be addressed to T. A. Hatton at tahatton@mit.edu.

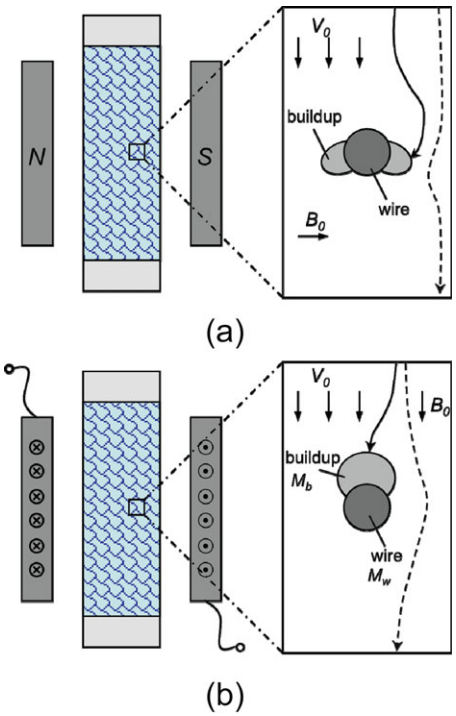

Figure 1. Basic configurations of the single-wire capture model.

Solid lines show the trajectories of captured magnetic particles and dashed lines show the trajectories of noncaptured particles. A permanent magnet is usually used for the transverse configuration and an electromagnet for the longitudinal configuration. Background flow speed is V_0 and background magnetic flux density is B_0. The buildup and iron wire are assumed to have uniform magnetizations that are parallel to the external magnetic field. [Color figure can be viewed in the online issue, which is available at wileyonlinelibrary.com.]

of the buildup radius, b_{La}, beyond which the contest between drag forces and magnetic forces is resolved in favor of the former. This critical value, b_{La}, is the limit of static buildup.[21,22] The model provides a very useful estimate of the maximum buildup for weakly magnetic particles; but it does not give an indication as to how long it takes to attain this state. In addition, because this model neglects the effect of particle buildup on the magnetic field, it cannot explain the sharp, spike-shaped profiles produced by strongly magnetic particles.[23,24]

In this article, we present a dynamic model for particle accumulation on a wire and we study how buildup growth influences the flow and magnetic fields. We treat the surface of the particle buildup as a moving interface. Such moving boundary problems can be found in a wide range of applications, including crystal growth, multiphase flow, metallic material erosion, plasma etching, and fluid-structure interactions.[25,26] In our model, the flow field and magnetic field are calculated by the finite element method (Comsol Multiphysics) at each simulation step. A particle trajectory model is used to calculate where and how frequently the particles deposit on the buildup surface under the influence of magnetic and flow fields, based on which the dynamic process of magnetic particle buildup growth is studied.

Model Development

Flow field, magnetic field, and particle trajectory

For the purposes of this article, we have considered a single magnetically susceptible wire, as illustrated in Figure 1. There are basically two configurations: a transverse configuration, in which the flow direction is perpendicular to the magnetic field and magnetic particles are trapped on the sides of the wire, and a longitudinal configuration, in which the flow direction is parallel to the magnetic field and magnetic particles are trapped on the top of the wire.[27] The magnetic particles are simply magnetic cores coated with a layer of polymer.[21] Figure 2 shows the simulation block used in this study. A Cartesian (x, y) reference frame is mounted at the center of the wire. Magnetic particles are uniformly released at boundary 1 ($y = L_2/2$) over the range $x = -L_1/2$ to $L_1/2$. When a magnetic particle enters the simulation block, it is subjected to five types of forces: magnetic, gravitational, hydrodynamic drag, Brownian thermal motion, and particle–particle interactions. The magnetic force is given by Eq. 1. The hydrodynamic drag force is described by Stokes' Law:[27]

$$\mathbf{F_h} = 6\pi\eta r_0(\mathbf{u} - \mathbf{v_p}) \tag{2}$$

where η is the fluid viscosity, r_0 is the particle radius, $\mathbf{u}$ is the background flow velocity at the location of the particle, and $\mathbf{v_p}$ is the particle velocity. In this work, we assume the magnetic particles to be of intermediate size (100 nm $< 2r_0 <$ 10 micron) and the particle suspension to be quite dilute (<1% volume fraction) so the Brownian, gravitational, and interparticle forces are negligibly small as compared with magnetic and fluid drag forces.

If the inertia of the particle may be neglected, we can write the governing equation for the particle trajectory as simply a balance between the magnetic force and the hydrodynamic force:

$$6\pi\eta r_0(\mathbf{u} - \mathbf{v_p}) = \mu_0 V_p M_p \nabla H \tag{3}$$

This equation is rendered nondimensional by choosing proper characteristic quantities: velocity is scaled by the inlet flow speed, V_0, length is scaled by wire diameter, $2a$, and magnetic intensity is scaled by B_0/μ_0, where B_0 is the magnitude of the uniform background magnetic field. The dimensionless form of Eq. 3 is then

$$\mathbf{v}_p^* = \kappa_{MF}(\nabla^* H^*) + \mathbf{u}^* \tag{4}$$

where

$$\kappa_{MF} = \frac{V_p M_p B_0}{12\pi\eta r_0 V_0 a} \tag{5}$$

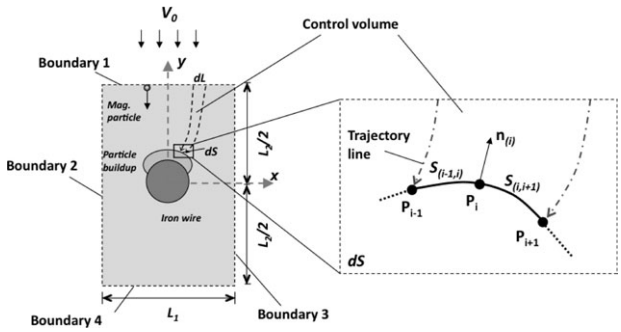

Figure 2. Simulation block for dynamic particle buildup growth showing the geometry, boundaries, and marker points.

The fluid motion is described by the equation of continuity and the Navier-Stokes equation, i.e.

$$\nabla^* \cdot \mathbf{u}^* = 0 \tag{6}$$

and

$$Re(\mathbf{u}^* \cdot \nabla^* \mathbf{u}^*) = \nabla^{*2} \mathbf{u}^* - \nabla^* \tilde{p}^*, \tag{7}$$

respectively, where $\tilde{p}^*$ is the dimensionless pressure and

$$Re = \frac{2\rho V_0 a}{\eta} \tag{8}$$

is the Reynolds number, in which ρ, the mass density of the particle suspension, is effectively the density of water for dilute conditions.

The magnetic field strength and magnetic flux density intensity are described by

$$\nabla^* \times \mathbf{H}^* = 0 \tag{9}$$

and

$$\nabla^* \cdot \mathbf{B}^* = 0$$

where

$$\mathbf{B}^* = \mathbf{B}/B_0 \tag{10}$$

The relation between **B*** and **H*** varies greatly depending on the domain.

In the flow subdomain:

$$\mathbf{B}^* = \mu_{r(\text{water})} \mathbf{H}^* \tag{11}$$

Because $\mu_{r(\text{water})}$, the relative permeability of the suspension, is very nearly one for dilute particle suspensions, we will generally replace **H*** by **B*** in this domain, i.e.

$$\mathbf{B}^* = \mathbf{H}^* \tag{12}$$

In the magnetic particle accumulation subdomain:

$$\mathbf{B}^* = \mathbf{H}^* + \mathbf{M}^* \text{ and } \mathbf{M}^* = \frac{\mu_0 M_b}{B_0} \left(\frac{\mathbf{B}^*}{|\mathbf{B}^*|} \right) = M_b^* \left(\frac{\mathbf{B}^*}{|\mathbf{B}^*|} \right) \tag{13}$$

In the wire subdomain:

$$\mathbf{B}^* = \mathbf{H}^* + \mathbf{M}^* \quad \text{and} \quad \mathbf{M}^* = \frac{\mu_0 M_w}{B_0} \left(\frac{\mathbf{B}^*}{|\mathbf{B}^*|} \right) = M_w^* \left(\frac{\mathbf{B}^*}{|\mathbf{B}^*|} \right) \tag{14}$$

In above equations, **M** is the magnetization and M_b and M_w are the volumetric magnetizations for the buildup and the wire, respectively. The volumetric magnetization of the wire is treated as a piece-wise continuous function:

$$M_w = \begin{cases} 2B_0/\mu_0 & \text{not magnetically saturated} \\ M_{w,sp} & \text{magnetically saturated} \end{cases} \tag{15}$$

where $M_{w,sp}$ is the intrinsic volumetric magnetization of the wire material. The result for the unsaturated case recognizes that the permeability of the wire is much greater than that of the surrounding fluid. The volumetric magnetization of the buildup M_b can be calculated approximately as

$$M_b = \phi_b M_p = \frac{4}{3} \pi r_0^3 n_s M_p \tag{16}$$

where ϕ_b is the volume fraction of magnetic particles in the buildup, and n_s is the particle number density in the buildup, which is equal to $1/(2r_0)^3$ for simple cubic dense packing. The particles are assumed to be saturated (i.e., fully aligned with the magnetic field) so that M_p is a constant. In our study, we assume that the magnetization of the wire and the buildup are both aligned with the background magnetic field, as expressed by Eqs. 12 and 13. Continuity is imposed at all interfaces, i.e.,

$$\mathbf{n_b} \cdot (\mathbf{B_1} - \mathbf{B_2}) = 0 \text{ and } \mathbf{n_b} \times (\mathbf{H_1} - \mathbf{H_2}) = 0 \tag{17}$$

where $\mathbf{n_b}$ is the outwardly directed unit normal vector, and subscripts 1 and 2 are used to distinguish different subdomains.

Conservation of mass

It is also necessary to describe the concentration of particles in the fluid. The concentration of the magnetic particles (defined as volume fraction ϕ) is governed by

$$\frac{\partial \phi}{\partial t} + \nabla \cdot (\mathbf{v_p} \phi) = 0 \tag{18}$$

where ϕ is the volumetric concentration of magnetic particles in the bulk suspension. The boundary conditions are

$$\phi = \phi_0 \tag{19}$$

on boundary 1, where ϕ_0 is the inlet concentration, and

$$-\phi \mathbf{v_p} \cdot \mathbf{n_b} = (\phi_b - \phi) v_{b,n} \tag{20}$$

on the buildup surface, where $\mathbf{n_b}$ is a unit vector denoting the outward normal to the surface dS, ϕ_b is the particle volume fraction in the buildup, and $v_{b,n}$ is the velocity of the buildup surface in the direction normal to itself. The boundary condition represented by Eq. 20 is the sole source of unsteadiness in the problem. It therefore determines the time constant for the system (buildup growth process). Given $\phi_b > \phi_0$, an expectation that ϕ will be of the same order as ϕ_0, and an expectation that $\mathbf{v_p}$ is of order V_0, it immediately follows that $v_{b,n}$ is of order $\left(\frac{\phi_0}{\phi_b}\right) V_0$, and the time constant is therefore $\tau_b = \frac{2a}{V_0} \left(\frac{\phi_b}{\phi_0}\right)$. Dimensionless time has accordingly been defined as

$$T^* = \frac{t}{\tau_b} \tag{21}$$

A similar analysis performed on Eq. 18 shows that the intrinsic time constant for a concentration change is of order $2a/V_0$. Thus, the system time constant is much longer than that for the concentration response, so the quasi-steady form of Eq. 18 is entirely adequate. One could now solve the quasi-steady version of Eq. 18, subject to Eq. 19, and then use Eq. 20 to obtain $v_{b,n}$.

As our only real interest is in $v_{b,n}$, this is cumbersome and we have chosen an equivalent, but slightly different, approach. The quasi-steady version of Eq. 18 merely states that the flow of particles into a control volume is equal to the flow of particles from the same control volume. It is convenient to define a control volume in which the sides are defined by particle trajectory lines (see Figure 2). Particles

Table 1. Domain and Boundary Settings (in Dimensionless Form)

Domain	Magnetostatic	Fluid Mechanics	Transport of Particles
Flow subdomain	$\nabla^* \cdot \mathbf{B}^* = 0$ $\nabla^* \times \mathbf{H}^* = 0$ $\mathbf{B}^* = \mathbf{H}^*$	Equations 6 and 7	$\left(\frac{\phi_u}{\phi_b}\right)\frac{\partial \phi}{\partial T^*} + \mathbf{v}_\mathbf{p}^* \cdot \nabla^* \phi = -\phi \nabla^* \cdot \mathbf{v}_\mathbf{p}^*$
Buildup subdomain	$\nabla^* \cdot \mathbf{B}^* = 0$ $\nabla^* \times \mathbf{H}^* = 0$ $\mathbf{B}^* = \mathbf{H}^* + \mathbf{M}^*$ $\mathbf{M}^* = M_\mathrm{b}^*\left(\frac{\mathbf{B}^*}{\lvert\mathbf{B}^*\rvert}\right)$	Inactive	Inactive
Wire subdomain	$\nabla^* \cdot \mathbf{B}^* = 0$ $\nabla^* \times \mathbf{H}^* = 0$ $\mathbf{B}^* = \mathbf{H}^* + \mathbf{M}^*$ $\mathbf{M}^* = M_\mathrm{w}^*\left(\frac{\mathbf{B}^*}{\lvert\mathbf{B}^*\rvert}\right)$	Inactive	Inactive
Boundary	**Magnetostatic**	**Fluid Mechanics**	**Transport of Particle**
Boundary 1	$B_x^* = 0$, $B_y^* = 1$	$u_x^* = 0$, $u_y^* = -1$	$v_{\mathrm{p},y}^* \cong 1$, $v_{\mathrm{p},x}^* \cong 0$, $\phi = \phi_0$
Boundaries 2 and 3	$B_x^* = 0$, $B_y^* = 1$	Impermeable, no stress	Impermeable
Boundary 4	$B_x^* = 0$, $B_y^* = 1$	Constant pressure	N/A
Buildup surface	Continuity	No slip	$-\phi \mathbf{v}_\mathbf{p}^* \cdot \mathbf{n}_\mathbf{b} = (\phi_\mathrm{b} - \phi) v_{\mathrm{b,n}}^*$
Wire surface	Continuity	No slip	Impermeable/Inactive
Buildup/wire interface	Continuity	Inactive	Inactive

flow into the volume across dL and leave at dS. The conservation statement is therefore

$$V_0 \phi_0 dL \cong -\phi\left(\mathbf{v}_\mathbf{p} \cdot \mathbf{n}_\mathbf{b}\right) dS \tag{22}$$

Equations 20 and 22 then give

$$v_{\mathrm{b,n}} = V_0 \frac{dL}{dS} \frac{\phi_0}{\phi_\mathrm{b} - \phi} \tag{23}$$

or, if $\phi_\mathrm{b} \gg \phi$,

$$v_{\mathrm{b,n}}^* = \frac{\phi_\mathrm{b}}{\phi_0} \frac{v_{\mathrm{b,n}}}{V_0} = \frac{dL^*}{dS^*} \tag{24}$$

To evaluate dL^*/dS^*, trajectories are determined for two nearby particles such that dL^* and dS^* may be obtained. The trajectories themselves are simply given by the usual Lagrangian relationship, i.e.,

$$\frac{d\mathbf{r}_\mathbf{p}}{dt} = \mathbf{v}_\mathbf{p} \tag{25}$$

A final integration of the velocity given by Eq. 24 provides an evaluation of the buildup as a function of position and time.

The model and relevant subdomain and boundary settings are summarized in Table 1. It is also important at this point to note the magnitudes of certain dimensionless parameters. Of these, the most important may be κ_MF, which may be viewed as the velocity induced by the magnetic field divided by V_0. The practical ranges of the various parameters are listed in Tables 2 and 3.

Problem discretization and front-tracking method

We have assumed that the magnetic particles have very poor mobility in the buildup so that the buildup does not restructure. The buildup surface is discretized and tracked explicitly by a series of marker points distributed evenly over the buildup surface, as shown in Figures 2 and 3.

The position of marker point P_i is updated in accordance with

$$\mathbf{P}_i^*(T^* + \Delta T^*) = \mathbf{P}_i^*(T^*) + v_{\mathrm{b,n}(i)}^* \mathbf{n}_{\mathrm{b}(i)} \Delta T^* \tag{26}$$

where $\mathbf{P}_i^*$ represents the position of point P_i, ΔT^* is the dimensionless time step, $\mathbf{n}_{\mathrm{b}(i)}$ is the outward unit vector normal to the buildup surface, and $v_{\mathrm{b,n}(i)}^*$ is the normal component of the velocity of the buildup surface at this marker point. Equation 26 is used to track the movement of marker points. As the buildup grows, the marker points may move closer together or further apart, and sometimes even cause topological changes, making redistribution of markers necessary. The modeling algorithm is shown in Figure 3. More detailed discussion of this process is available in Chen.[28]

We use very densely distributed marker points, with an average distance between two adjacent maker points of about $0.01a$. Fluid is assumed to cross boundary 1 with a uniform downward velocity V_0. Magnetic particles cross the boundary with a velocity equal to that of the fluid. A constant pressure condition is applied on boundary 4.

Table 2. Practical Operating Parameters

Parameter	Range
Diameter of magnetic particle $2r_0$	$0.05 - 2$ μm
Background magnetic flux density B_0	$0.1 - 2$ Tesla
Saturated magnetization of core (magnetite) σ_sp	78 $\mathrm{Am^2/kg}$
Diameter of magnetizable wire $2a$	50–2000 μm
Magnetization of wire $\mu_0 M_\mathrm{w}$	0–2 Tesla
Inlet velocity V_0	0.5–10 cm/s
Volume concentration of particles in feed ϕ_v	0.001–1%

Table 3. Ranges of Dimensionless Numbers

Dimensionless Numbers	Practical Range	In Our Simulation
Reynolds number Re	0.1–200	1–50
Dimensionless magnetic velocity κ_MF	0.001–1000	0.2–4
ϕ_0/ϕ_b	2×10^{-4} to 2×10^{-2}	$<<1$
M_b^*	0–1	0–0.132
M_w^*	0–2	2

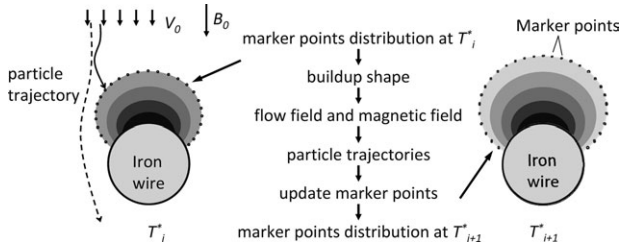

Figure 3. Modeling algorithm showing the calculation procedure within a single time step.

Results and Discussion

Buildup shape evolution

We first show that the magnetic properties of the buildup exert an important influence on the evolution of the buildup morphology. Figures 4a, b depict the buildup process for longitudinal and transverse configurations, respectively, for $Re = 1$, $\kappa_{MF} = 1$, and $M_b^* = 0$. Each contour line corresponds to a buildup shape at a certain time. The time steps are chosen so that at each step the maximum increment in buildup thickness is equal to one-tenth of the wire radius. The buildup shapes obtained are very similar to those observed experimentally with weakly paramagnetic particles.[20,23]

Figures 4c, d depict the buildup process for the same longitudinal and transverse configurations, but the effect of particle buildup on magnetic field is considered. The resulting buildup shapes exhibit a spiky dendritic pattern. Formation of a single on-axis spike has been observed experimentally when strongly magnetic particles are used (Fe_3O_4).[23] The static particle buildup model developed by Nesset and Finch[20] does not allow for this behavior and is, therefore, not applicable to the capture of strongly magnetic particles. In fact, when strongly magnetic particles such as ferromagnetic or superparamagnetic particles are used, the buildup is itself a magnet and this distorts the original field. In this case, the magnetic field distribution changes with time and must be updated at each calculation step.

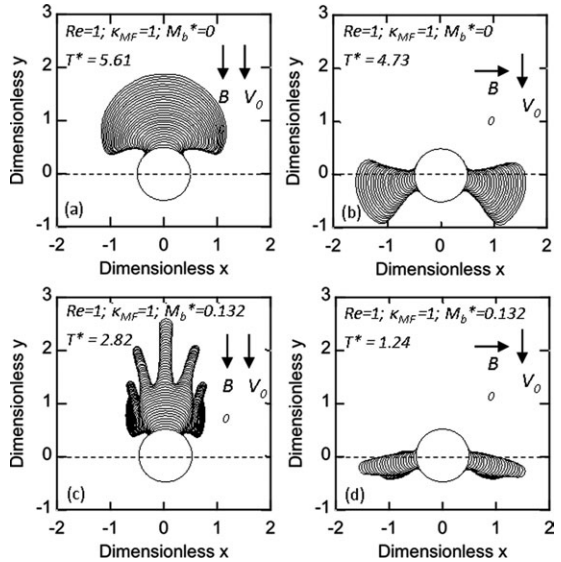

Figure 4. Magnetic particle buildup evolution process for cases without the effect of buildup on magnetic field for the (a) longitudinal and (b) transverse configurations; and cases with the effect of buildup on magnetic field for the (c) longitudinal and (d) transverse configurations.

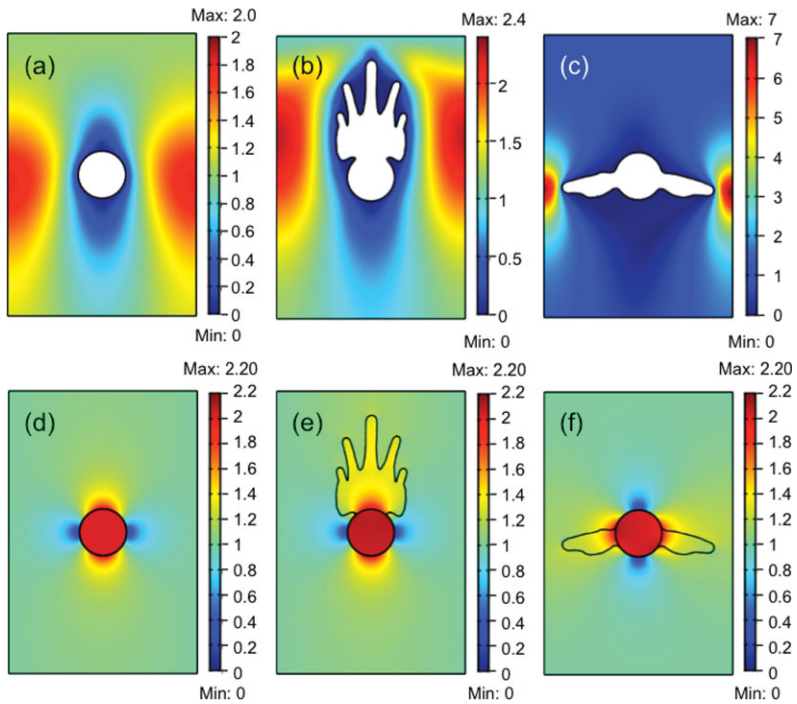

Figure 5. Effect of particle buildup on the wire on the flow and magnetic field distributions.

The magnitude of the dimensionless velocity at (a) $T^* = 0$, (b) $T^* = 2.82$ for longitudinal configuration, and (c) $T^* = 1.24$ for the transverse configuration. Note that the intensity scales are different in each of the figures. The distribution of the dimensionless magnetic flux density magnitude at (d) $T^* = 0$ and (e) $T^* = 2.82$ for the longitudinal configuration, and (f) at $T^* = 1.24$ for the transverse configuration. The values of dimensionless parameters used in simulation are $Re = 1$, $\kappa_{MF} = 1$, $M_b^* = 0.132$, $L_1^* = 4$, and $L_2^* = 6$. [Color figure can be viewed in the online issue, which is available at wileyonlinelibrary.com.]

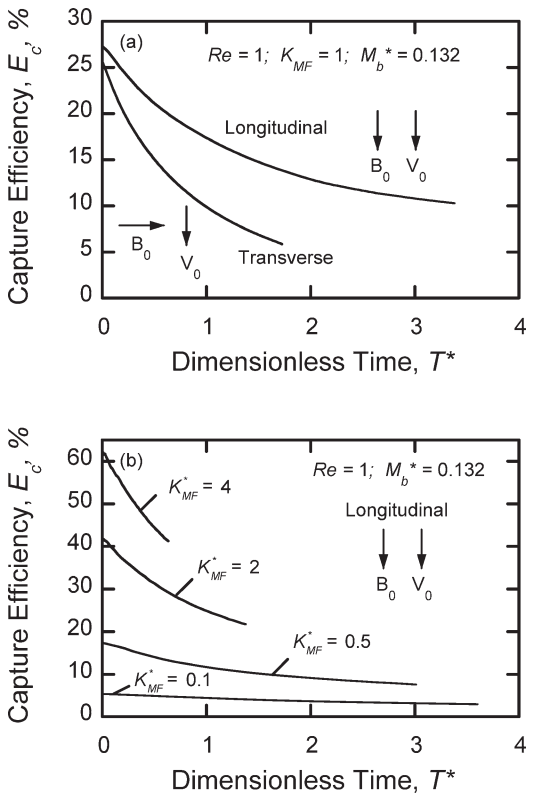

Figure 6. The capture efficiency decreases monotonically with dimensionless time for (a) different configurations, and (b) different values of κ_{MF}.

The fixed parameter values in these simulations were $Re = 1$, $M_b^* = 0.132$, $L_1^* = 4$, and $L_2^* = 6$.

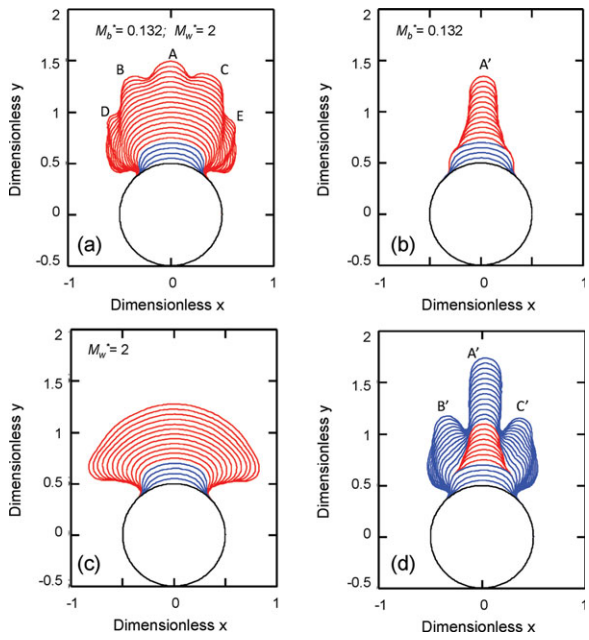

Figure 7. Effect of changes in magnetization of the buildup and the wire on the evolution of the magnetic particle buildup with time for (a) $M_b^* = 0.132$ and $M_w^* = 2$ throughout the test; (b) $M_b^* = 0.132$ and $M_w^* = 2$ before the 5th step ($T^* = 0.11$), and $M_w^* = 0$ for the rest of test; (c) $M_b^* = 0.132$ and $M_w^* = 2$ before the 5th step ($T^* = 0.11$), and $M_b^* = 0$ for the rest of test; (d) Continuation of (b) but with $M_w^* = 2$ after the 10th step ($T^* = 1.22$).

[Color figure can be viewed in the online issue, which is available at wileyonlinelibrary.com.]

Influence of buildup on flow field, magnetic field, and capture efficiency

Figure 5 shows the flow and magnetic field distributions (in dimensionless magnitude) at $T^* = 0$ and $T^* = 2.82$ (for longitudinal configuration), or $T^* = 1.24$ (for transverse configuration), and provides an indication of how the buildup distorts these fields. As the buildup grows, it essentially increases the dimension of the "wire" (especially for the transverse configuration shown in Figure 5c) and the gradient of the magnetic field at the surface of the buildup decreases steadily, provided that $M_w > M_b$. Incoming particles are, therefore, subject to a smaller and smaller magnetic force as the buildup grows, and

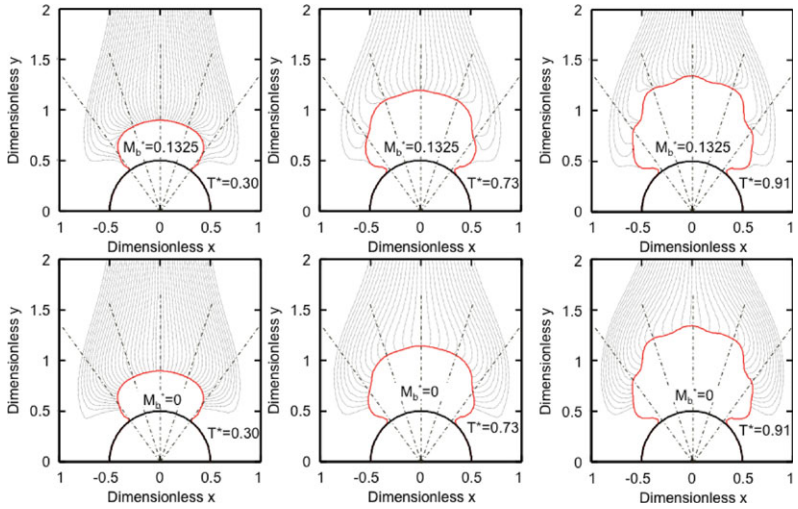

Figure 8. Magnetic particle trajectories at different times.

First row: trajectories for $M_b^* = 0.132$, $Re = 1$, $\kappa_{MF} = 1$, $L_1^* = 4$, and $L_2^* = 6$. Dashed straight lines correspond to angles of 0.3π, 0.4π, 0.5π, 0.6π, and 0.7π. Second row: trajectories if buildup magnetization were assumed to be zero at that instance. [Color figure can be viewed in the online issue, which is available at wileyonlinelibrary.com.]

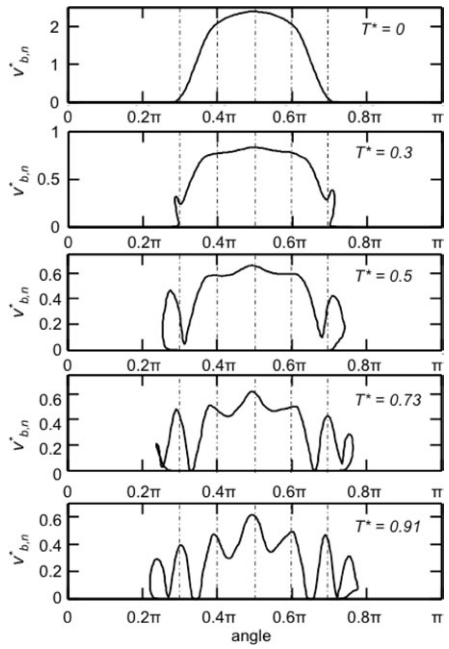

Figure 9. The normal component of the buildup surface velocities $v_{b,n}^*$ as a function of position (represented as angle) on the buildup, at different times.

$M_b^* = 0.132$, $Re = 1$, $\kappa_{MF} = 1$, $L_1^* = 4$, and $L_2^* = 6$.

are less likely to be captured by the wire. This has a negative effect on capture efficiency, defined as

$$E_c = \frac{\text{Number of particles captured}}{\text{Total number of particles released}} \tag{27}$$

which is shown in Figure 6 as a function of time for selected operating conditions.

Figure 5 shows that the buildup growth changes the geometry much faster for the transverse configuration than it does for the longitudinal configuration, which explains why the capture efficiency shown in Figure 6a decreases much more rapidly for the transverse than for the longitudinal configuration. In addition, Figure 6b shows that capture efficiency drops much faster for larger values of κ_{MF}. It might be noted that the scaling for T^* was developed under the assumption that v_p and V_0 are nearly equal. This implies that κ_{MF} is close to or less than unity. For large values of κ_{MF}, it would be better to multiply the right-hand side of Eq. 21 by κ_{MF}. This was not done here because κ_{MF} is typically of order one in most applications.

Reason for onset of dendritic buildup growth

As is clear from the results for the longitudinal configuration in Figure 4c, the buildup growth process can be divided into two regimes. In the early stages, the buildup grows nearly uniformly in all directions within the attractive zone, much as in the case where $M_b^* = 0$, Figure 4a. Later, the smooth buildup surface develops a number of dendrites. The transition from the first regime to the second regime is a gradual process. In this section, we examine the onset of dendritic buildup growth in depth.

We first explored the different roles of the wire and the buildup. The results are shown in Figure 7, where buildup profiles before the 5th step are shown in blue and in red for subsequent steps. All tests were done for $Re = 1$, $\kappa_{MF} = 1$, $L_1^* = 4$, and $L_2^* = 6$. The result for the first test, where $M_b^* = 0.132$ and $M_w^* = 2$, is shown in Figure 7a, which is the same as Figure 4c. In the second test, M_w^* was set to 0 after the fifth step. From Figure 7b, we see that only one dendrite (named A′) developed. The third test was designed to assess the role of the buildup magnetization. The wire magnetization M_w^* was kept at 2 for all times, but M_b^* was switched to 0 after the fifth time step. Figure 7c shows that the result is a smoothly growing front for the rest of the experiment. The fourth test is the same as the second, but M_w^* was switched back to 2 after the tenth step. The presence of dendrite A′ significantly alters the surrounding magnetic field, with a strong magnetic field gradient at its tip. The result is that magnetic particles tend to deposit either at the top of dendrite A′ or at some distance from it. As shown in Figure 7d, dendrite A′ kept growing but the wire magnetization also led to development of dendrites B′ and C′.

Figure 8 shows the trajectory lines of magnetic particles at different times. The first row shows results for $M_b^* = 0.132$, $Re = 1$, $\kappa_{MF} = 1$, $L_1^* = 4$, and $L_2^* = 6$ In the second row, trajectory lines are those that would exist if M_b^* were suddenly switched to zero at that instant. Thus, Figure 8 is a more detailed exploration of the issues raised by Figure 7b. The results indicate that there are no preferential deposition areas if the magnetization of the buildup is assumed to be zero, even at $T^* = 0.91$ when dendritic growth is already apparent. However, as shown in the first row, magnetization

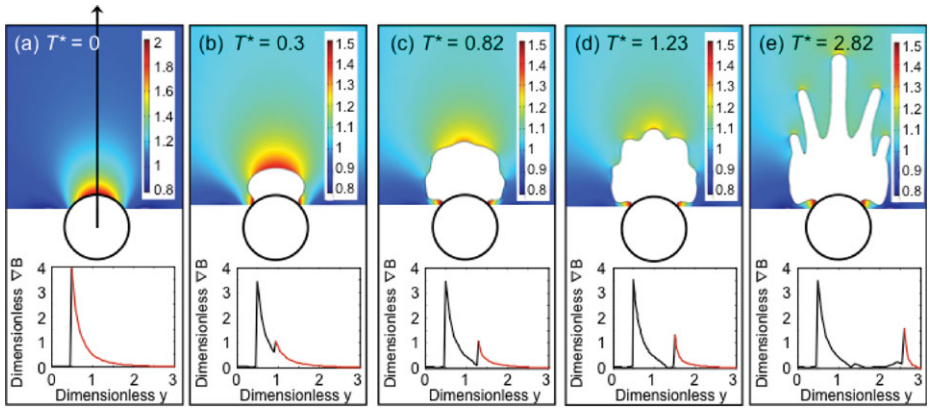

Figure 10. Buildup shape (white), dimensionless magnetic flux density (color), and dimensionless magnetic field gradient along the *y* axis (graphs) at different times.

$Re = 1$, $M_b^* = 0.132$, $L_1^* = 4$, and $L_2^* = 6$. [Color figure can be viewed in the online issue, which is available at wileyonlinelibrary.com.]

of the buildup significantly changes the trajectory lines. Up to $T^* = 0.30$, preferential deposition is limited to the top of the buildup. At this time, the preferential deposition area is quite large and covers almost the entire top surface of the buildup. At $T^* = 0.73$, two additional sites of preferential deposition are apparent. By $T^* = 0.91$, the number of preferential deposition areas has increased to five. These areas develop into the five dendrites A, B, C, D, and E that we have seen in Figure 7a. In the first row, dashed lines have been included at 0.3π, 0.4π, 0.5π, 0.6π, and 0.7π. These were inserted in part as guides to the eye, but they also roughly correspond to the positions of preferential deposition. Figure 9 shows the value of $v_{b,n}{}^*$ as a function of position (denoted by angle, $\pi/2$ corresponds to the topmost point on the buildup surface), at different times. At $T^* = 0$, when no buildup is present, particles deposit relatively evenly on the region between 0.3π and 0.7π, with the highest deposition rate at $\pi/2$, and there is no secondary preferential deposition area. As the buildup grows, two rather broad secondary maxima emerge around 0.4π and 0.6π. Rather sharp, very local, maxima also appear at about 0.3π and 0.7π, whereas the global maximum remains at $\pi/2$. After $T^* = 0.73$, the preferential deposition areas further develop into the above mentioned dendrites A, B, C, D, and E, corresponding approximately to the positions of $\pi/2$, 0.4π, 0.6π, 0.3π, and 0.7π, respectively. Dashed vertical lines corresponding to each of the angles are shown; and, as before, local maxima are found near these angular positions. Although new local maxima are also found around 0.25π and 0.75π after $T^* = 0.73$, no significant dendritic growth is observed around these areas up to $T^* = 0.91$. The local maxima and minima also move slightly toward the center line as time proceeds. Because the shape of the surface is a time average of past deposition rates, this slow drift produces broader peaks and valleys than would otherwise be observed if there was no such drift.

Figure 10 shows the magnetic field distribution in the entire region at different times for $Re = 1$, $\kappa_{MF} = 1$, and $M_b^* = 0.132$, together with the corresponding dimensionless magnetic field gradients along the centerline. On the dimensionless magnetic field gradient graphs, the gradient inside the buildup is shown in black, and outside the buildup in red. As seen from Figure 10a, initially the field gradient is dominated by the contribution from the wire; but the contributions from the wire and the buildup become comparable when the buildup thickness is about equal to the radius of the wire, as seen in Figure 10b. If the buildup thickness is equal to, or greater than, the diameter of the wire (see Figure 10c), the dominant contributor to the field gradient is the buildup itself. Perturbations to the smooth surface then become unstable and a dendritic conformation is the result.

Parametric study

Figure 11a shows the influence of effective dimensionless buildup magnetization (M_b^*) on buildup shape evolution. With increasing buildup magnetization, the buildup becomes thinner in the transverse direction (x direction in this case) and the onset of dendrite formation begins earlier. The total number of dendrites also decreases as M_b^* increases. When M_b^* is sufficiently large, e.g., $M_b^* = 1$, only one dendrite is obtained within the time range studied. To facilitate comparison, the final dimensionless times are chosen such that the heights of the buildup are about 2. Figure 11b shows

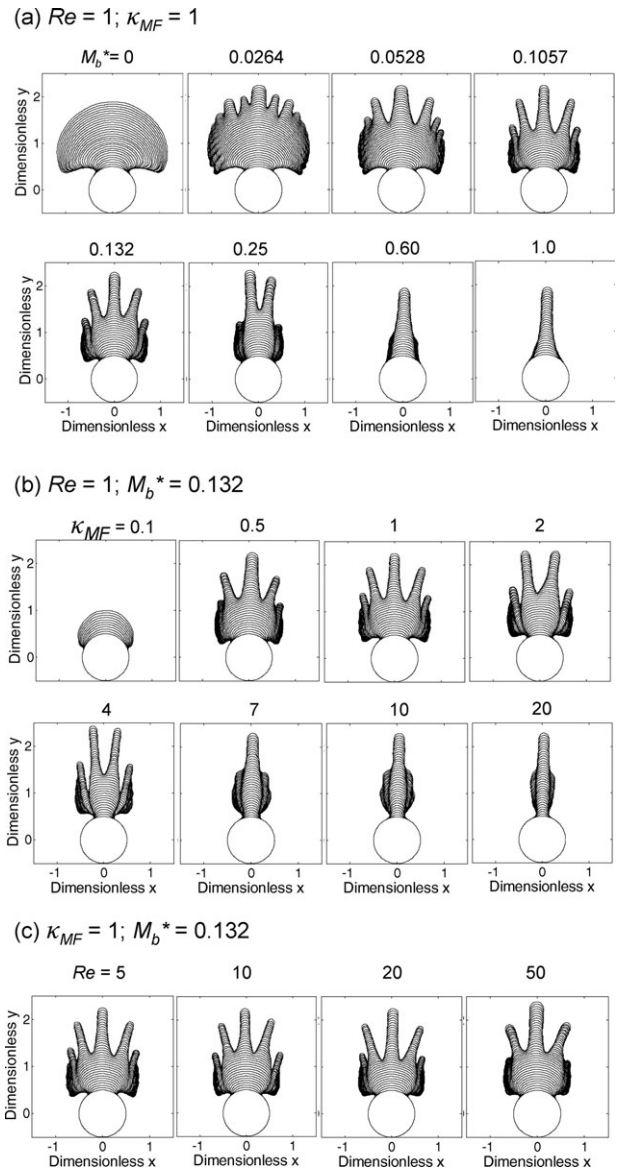

Figure 11. Results of parametric study for the longitudinal configuration: (a) Influence of M_b^*; (b) Influence of κ_{MF}; (c) Influence of Re with fixed κ_{MF}.

Initial geometry: $L_1^* = 4$, and $L_2^* = 6$; some graphs are replotted for better comparison.

the influence of κ_{MF} at fixed Re and M_b^*. The total number of dendrites varies from 5 to only 1 over a large range of κ_{MF}. When κ_{MF} is small, dendritic growth does not occur because the single-wire capture efficiency is very low and the buildup volume is never sufficient for the magnetic field to be dominated by the contribution from the buildup material. This may be seen in the first graph of Figure 11b, for which the final dimensionless time is $T^* = 7.2$ and the buildup growth process is very close to steady state.

Figure 11c shows the influence of Re at fixed κ_{MF} and M_b^*. Buildup shape does not vary much amongst these graphs, which indicates that the dynamic process of particle buildup growth is less dependent on Re than on κ_{MF} and M_b^*. This confirms our separate study where we have found that it is κ_{MF} that has a key influence on particle trajectory and capture.[28]

Although the parametric study performed above yields an odd number of dendrites in all reported cases, an even dendrite

Table 4. Experimental Settings and Parameters

	Parameters	Setting 1	Setting 2
Particle properties	Material	Manganese pyrophosphate ($Mn_2P_2O_7$)	Magnetite (Fe_3O_4)
	Magnetic property	Paramagnetic	Ferromagnetic
	Mass magnetization σ_{sp}	1.014 Am^2/kg	40 Am^2/kg
	Density	3710 kg/m^3	5150 kg/m^3
	Average diameter	8 μm	10 μm
	Radius ratio	1	1
Wire properties	Material	Nickel	Nickel
	Magnetic property	Ferromagnetic	Ferromagnetic
	Magnetization, $\mu_0 M_w$	0.6 Tesla	0.12 Tesla
	Diameter	125 μm	125 μm
Operating parameters	Inlet particle concentration	0.4 g/L	0.1 g/L
	Inlet velocity V_0	3.81 cm/s	1.38 cm/s
	Background magnetic flux density	1 Tesla	0.06 Tesla
	Characteristic time for buildup growth: $(\phi_b/\phi_0)(2a/V_0)$	16 s	244 s
	Time at which buildup shape is observed	$T = 120$ s or $T^* = 7.5$	$T = 120$ s or $T^* = 0.5$
Dimensionless Numbers	Re	4.76	1.72
	κ_{MF}	0.42	20
	M_b^*	0.0079	1.124

number can also result. Instead of a single large dendrite at $\pi/2$, two equally large dendrites develop on either side of $\pi/2$.

Comparison with experimental results

Friedlaender and Takayasu have shown experimentally that buildup shapes depend on the type of magnetic particles, i.e., whether they are weakly or strongly magnetic.[23,24] We have compared their experimental results with our simulations for the operating parameters shown in Table 4. These two settings were chosen because they include both longitudinal and transverse configurations, and both weakly and strongly magnetic particles.

Figure 12a shows the results for weakly magnetic particles in a transverse field. The simulated buildup evolution profiles are shown as solid lines whereas the experimental buildup profile is shown as a dashed line. The final buildup profiles correspond to $T^* = 7.5$. The simulation result gives a buildup pattern quite similar to the experimental result, with certain differences in the upwind and downwind areas of the buildup.

Figure 12b shows the comparison for strongly magnetic particles in a longitudinal field. Both experiment and simulation give a sharp peak. The final buildup profiles correspond to $T^* = 0.5$. Although there are some discrepancies in the buildup shapes, it is evident that the model captures the most important features of the process and provides added insight concerning the evolution of the buildup shape. We are not aware of any experimental results that have reported multiple dendrites of the sort found in this work. This may be due to the formation of particle chains in the suspension, whereas this analysis has assumed that each particle acts independently of every other particle.

Concluding Remarks

We have developed a dynamic model to study magnetic particle accumulation processes on a single wire in HGMS. For a given geometry and initial conditions, the dynamic buildup growth process can be described completely by three dimensionless numbers: κ_{MF}, Re, and M_b^*. The model is used to study the evolution of buildup shape with time, and the influence of buildup on flow field and magnetic field. Parametric study shows that κ_{MF} and M_b^* are the key dimensionless numbers in determining the resulting buildup shapes, whereas the effect of Re is small. The results show that the capture efficiency decreases dramatically as particles accumulate on the wire surface and the growing accumulation of particles significantly distorts both the surrounding flow and magnetic fields. It is also shown that, under certain conditions, the interface between the buildup and the fluid is unstable and that dendrites are therefore produced. If M_b^* is small, the buildup has a smoothly growing front and no dendritic growth is obtained. As M_b^* increases, a smoothly growing front is observed at short times because the magnetic field distribution is dominated by the wire. However, at later times, the buildup material provides the dominant contribution to the magnetic field and the front becomes unstable. The simulated buildup shapes obtained at very low M_b^* values are very similar to those found experimentally with very weakly paramagnetic particles. When large M_b^* values are used in our simulation, we were

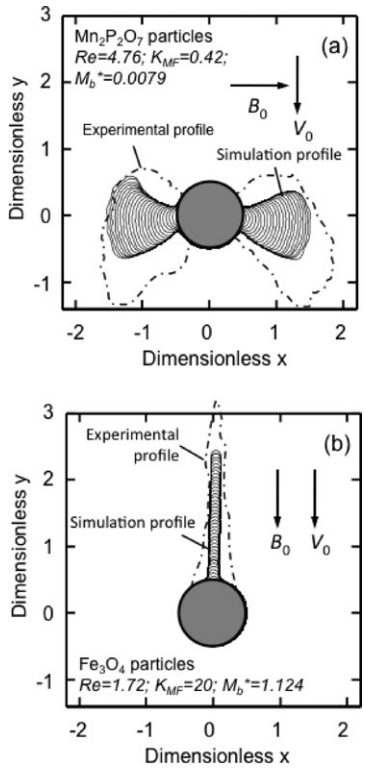

Figure 12. Comparison of simulation and experimental results.

able to predict the single-spike buildup shape reported in previous experiments with strongly magnetic particles.

These results provide insights as to the optimal duration of a collection interval. Presumably, collection should be terminated if (a) the efficiency has been severely impaired, or (b) the cross section for flow has been significantly reduced, or (c) the dendrites are likely to break with a consequent loss of product. Figure 6 suggests that collection times should be limited to values of T^* of order one unless κ_{MF} is quite low. Otherwise, collection efficiency suffers. As for obstruction of the cross section for flow, results such as those shown in Figure 4 may be compared with the lateral distance between wires (or the results may be used to select the distance between wires). On the basis of these results, the likelihood of dendrite breakage cannot be assessed unequivocally. However, one might guess that the situation shown in Figure 10d would be acceptable whereas that shown in Figure 10e represents an unacceptable risk.

Acknowledgments

The authors would like to acknowledge DuPont-MIT Alliance (DMA) for funding. They also thank Dr. Makoto Takayasu of the Plasma Science and Fusion Center of MIT for useful discussions and providing the experimental results.

Literature Cited

1. Kelland DR. High Gradient magnetic separation applied to mineral beneficiation. *IEEE Trans Magn*. 1973;MAG9:307–310.
2. Veasey TJ, Wilson RJ, Squires DM. *The Physical Separation and Recovery of Metals from Waste*. Amsterdam: Gordon and Breach Publishers, 1993.
3. Vanvelsen AFM, Vandervos G, Boersma R, Dereuver JL. High-gradient magnetic separation technique for waste-water treatment. *Water Sci Technol*. 1991;24:195–203.
4. Xia N, Hunt TP, Mayers BT, Alsberg E, Whitesides GM, Westervelt RM, Ingber DE. Combined microfluidic-micromagnetic separation of living cells in continuous flow. *Biomed Microdevices*. 2006;8: 299–308.
5. Inglis DW, Riehn R, Sturm JC, Austin RH. Microfluidic high gradient magnetic cell separation. *J Appl Phys*. 2006;99:08K101–08K101-3.
6. Bucak S, Jones DA, Laibinis PE, Hatton TA. Protein separations using colloidal magnetic nanoparticles. *Biotechnol Prog*. 2003;19: 477–484.
7. Franzreb M, Siemann-Herzberg M, Hobley TJ, Thomas ORT. Protein purification using magnetic adsorbent particles. *Appl Microbiol Biotechnol*. 2006;70:505–516.
8. Ditsch A, Yin J, Laibinis PE, Wang DIC, Hatton TA. Ion-exchange purification of proteins using magnetic nanoclusters. *Biotechnol Prog*. 2006;22:1153–1162.
9. Hobley TJ, Ferre H, Gomes CSG, Hansen DB, Petersen TL, Buus S, Thomas ORT. Advances in high-gradient magnetic fishing for downstream and bioprocessing. *J Biotechnol*. 2005;118:S56–S56.
10. Hubbuch JJ, Matthiesen DB, Hobley TJ, Thomas ORT. High gradient magnetic separation versus expanded bed adsorption: a first principle comparison. *Bioseparation*. 2001;10:99–112.
11. Watson JHP, Ellwood DC. Biomagnetic separation and extraction process for heavy-metals from solution. *Miner Eng*. 1994;7:1017–1028.
12. Moeser GD, Roach KA, Green WH, Laibinis PE, Hatton TA. Water-based magnetic fluids as extractants for synthetic organic compounds. *Ind Eng Chem Res*. 2002;41:4739–4749.
13. Gijs MAM. Magnetic bead handling on-chip: new opportunities for analytical applications. *Microfluid Nanofluidics*. 2004;1:22–40.
14. Rosensweig RE. *Ferrohydrodynamics*. New York: Dover Publications, 1997.
15. Friedlaender FJ, Takayasu M, Rettig JB, Kentzer CP. Particle flow and collection process in single wire HGMS studies. *IEEE Trans Magn*. 1978;14:1158–1164.
16. Simons WH, Treat RP. Particle trajectories in a lattice of parallel magnetized fibers. *J Appl Phys*. 1980;51:578–588.
17. Watson JHP. Magnetic filtration. *J Appl Phys*. 1973;44:4209–4213.
18. Chen HT, Ebner AD, Rosengart AJ, Kaminski MD, Ritter JA. Analysis of magnetic drug carrier particle capture by a magnetizable intravascular stent: 1. Parametric study with single wire correlation. *J Magn Magn Mater*. 2004;284:181–194.
19. Liu YA, Oak MJ. Studies in magnetochemical engineering. 2. theoretical development of a practical model for high-gradient magnetic separation. *AIChE J*. 1983;29:771–779.
20. Nesset JE, Finch JA. The static (buildup) model of particle accumulation on single wires in high-gradient magnetic separation—experimental confirmation. *IEEE Trans Magn*. 1981;17:1506–1509.
21. Ditsch A, Lindenmann S, Laibinis PE, Wang DIC, Hatton TA. High-gradient magnetic separation of magnetic nanoclusters. *Ind Eng Chem Res*. 2005;44:6824–6836.
22. Moeser GD, Roach KA, Green WH, Hatton TA, Laibinis PE. High-gradient magnetic separation of coated magnetic nanoparticles. *AIChE J*. 2004;50:2835–2848.
23. Friedlaender FJ, Takayasu M. Video recording of particle trajectories and buildup of single wires in high gradient magnetic separations. *International Conference on Industrial Applications of Magnetic Separation*. Franklin Pierce College: New Hampshire, 1978.
24. Friedlaender FJ, Takayasu M. A study of the mechanisms of particle buildup on single ferromagnetic wires and spheres. *IEEE Trans Magn*. 1982;18:817–821.
25. Tan LJ, Zabaras N. A level set simulation of dendritic solidification with combined features of front-tracking and fixed-domain methods. *J Comput Phys*. 2006;211:36–63.
26. Tryggvason G, Bunner B, Esmaeeli A, Juric D, Al-Rawahi N, Tauber W, Han J, Nas S, Jan YJ. A front-tracking method for the computations of multiphase flow. *J Comput Phys*. 2001;169:708–759.
27. Svoboda J. *Magnetic Techniques for the Treatment of Materials*. Dordrecht: Kluwer Academic Publishers, 2004.
28. Chen F. Magnetically enhanced centrifugation for continuous biopharmaceutical processing. PhD Thesis, Massachusetts Institute of Technology, Cambridge, MA, 2009.

Manuscript received Feb. 5, 2011, and revision received Sept. 21, 2011.